Effects of thiophene-fused isomer on high layered crystallinity in π-extended and alkylated organic semiconductors

Toshiki Higashino,*[a] Satoru Inoue,[b] Shunto Arai,[b,c] Seiji Tsuzuki,[b] Hiroyuki Matsui,[d] Reiji Kumai,[e] Kiyofumi Takaba,[f] Saori Maki-Yonekura,[f] Hirofumi Kurokawa,[g] Ichiro Inoue,[f] Kensuke Tono,[f,h] Koji Yonekura,[f,g] and Tatsuo Hasegawa[b]

[a] Research Institute for Advanced Electronics and Photonics, National Institute of Advanced Industrial Science and Technology (AIST), Tsukuba, Ibaraki 305-8565, Japan

[b] Department of Applied Physics, The University of Tokyo, Hongo, Tokyo 113-8656, Japan

[c] Research Center for Macromolecules and Biomaterials, National Institute for Materials Science (NIMS), Tsukuba, Ibaraki 305-0044, Japan

[d] Research Center for Organic Electronics, Yamagata University, Yonezawa, Yamagata 992-8510, Japan

[e] Condensed Matter Research Center (CMRC) and Photon Factory, Institute of Materials Structure Science, High Energy Accelerator Research Organization (KEK), Tsukuba, Ibaraki 305-0801, Japan

[f] RIKEN SPring-8 Center, Kouto, Sayo, Hyogo 679-5148, Japan

[g] Institute of Multidisciplinary Research for Advanced Materials, Tohoku University, Katahira, Aoba-ku, Sendai 980-8577, Japan

[h] Japan Synchrotron Radiation Research Institute, 1-1-1 Kouto, Sayo, Hyogo, 679-5198, Japan

ABSTRACT: Here we systematically investigated the effects of thiophene-fused isomer and the end-cap substitution on high layered crystallinity, film formability, and field-effect transistor characteristics in π-extended and alkylated organic semiconductors (OSCs). We developed four kinds of unsymmetric rod-like OSCs based on syn-/anti-isomers of benzothieno[6,5-*b*]-/benzothieno[5,6-*b*]-benzothieno[3,2-*b*]thiophene (BTBTT) with phenyl/alkyl substitutions with different alkyl chain lengths; **synCn** and **antiCn** (*n* = 6, 10). The layered molecular packing motifs of the compounds are distinct by the thiophene orientation of isomeric π-cores but are unaffected by the alkyl chain length. The **synCn** forms a *bilayer-type* layered herringbone (*b*-LHB) packing composed of *head-to-head* arrangement of unidirectionally-aligned molecular layers with showing high layered crystallinity and high carrier mobility over 10 $cm^2 V^{-1} s^{-1}$. By contrast, the **antiCn** forms *antiparallel alkyl-interdigitated* herringbone (*aai*-HB) structure in which the respective π-core layer is composed of alternating antiparallel alignment of π-cores and the alkyl chains are interdigitated with each other between the adjacent π-core layers. The latter shows relatively poor crystalline-film formability and moderate carrier mobility. Dispersion-corrected density functional theory calculations of intermolecular interaction energy reveal that the overall shape of the rigid π-core components is crucial for achieving unidirectionally-aligned and closely-packed 2D π-core layers, and that the flexible end-cap substituents strengthen and balance the layered crystallinity. The findings will be crucial for designing and developing the highly layered crystalline and high-performance OSCs.

INTRODUCTION

Fused-ring π-electron skeletons (or π-cores) based on thienoacenes constitute the fundamental material bases of organic semiconductors (OSCs) towards versatile electronics applications.[1-4] Among them, linearly extended π-cores, fused in acene-/phenacene-like manners, frequently form self-organized two-dimensional (2D) layered molecular packing that is optimal for efficient 2D carrier transport in organic field-effect transistors (OFETs).[5-7] Some OSCs based on linear π-cores exhibit superior film-forming ability (denoted as layered crystallinity) in solution and thus afford high-performance printed OFETs.[8-21] However, many similar molecules do not show the high layered crystallinity, or do not afford excellent device characteristics even if the layered assembly is achieved.[22-29] It is quite important to establish how to design and develop the OSC molecules showing efficient carrier transport as well as high layered crystallinity in the OSC molecules.

The carrier transport characteristics are primarily determined by the packing motifs of π-core components, which could be tuned by the modulation of π-cores and/or side-chain components in the OSC molecules. Recently, it was shown

that the layered crystallinity is considerably enhanced by end-cap substitutions with long alkyl chains and/or phenyl groups, as is demonstrated for some linear π-cores, such as benzothieno[3,2-*b*][1]benzothiophene (BTBT).[30-33] The unsymmetrically substituted molecules frequently form *bilayer-type* layered herringbone (*b*-LHB) packing, composed of *head-to-head* arrangement of unidirectionally-aligned monomolecular layers, eventually affording high layered crystallinity.[34-39] In the crystals, substituted long alkyl chains form alkyl chain layers which synergetically enhance the LHB packing of unidirectionally-aligned π-core layers.[40,41] The phenyl groups also assist the formation of the LHB packing motif. In particular, these end-cap effects allow to form *b*-LHB packing even for the unsymmetric π-cores whose unsubstituted moieties crystallize into antiparallel side-by-side arrangements.[42]

In contrast to the end-cap effects, little is known on the modulation effect of π-cores on the layered crystallinity and carrier transport characteristics. This is partly related to the difficulty in isolating thiophene-fused isomers of the π-cores in chemical syntheses.[43-57] It is also anticipated that the isomeric thiophene part easily presents positional disorder in the crystals.[58-60] Nonetheless, there exists a vast variety of structural isomers in candidate π-cores depending on the connecting pattern of the benzene and thiophene rings, even if they are limited to linear π-cores.[61-66] It is still unclear how such structural isomerism affects the intermolecular contact and transport characteristics, though it holds great promise in molecular design towards realizing practical high-performance OSCs.

In this study, we focus on the structural isomeric effect of BTBTT (BTBTT: benzothieno[6,5-*b*]benzothieno[3,2-*b*]thiophene, Scheme 1(a)); the orientation of terminal thiophene moiety can be changed to syn- and anti-forms.[67,68] We developed pure syn-/anti-thiophene-fused isomers of BTBTT-based OSCs with end-capped substitutions with phenyl and alkyl groups. The syn/anti isomerization in the BTBTT skeleton leads to the variation of reorganization energy, one of the critical factors defining carrier transport properties (Figure S1). We found that the **synCn** forms the *b*-LHB packing with showing high layered crystallinity and high mobility, whereas the **antiCn** presents a unique *antiparallel alkyl-interdigitated* herringbone (*aai*-HB) packing with showing poor film-forming ability and moderate mobility. Based on the results and on the quantum chemical intermolecular interaction calculations, we discuss the origin of the isomeric effect on the layered crystallinity of the OSC molecules in terms of the molecular geometry and the intermolecular forces.

RESULTS AND DISCUSSION

Material synthesis. Synthetic strategy for the target Ph-BTBTT-Cn derivatives is illustrated in Scheme 1(b). It shows two alternative synthetic routes, as classified in terms of final thiophene-ring formation reaction.[69,70] The first one, which was reported previously, has a demerit, as it inevitably affords undesirable product associated with the two possible

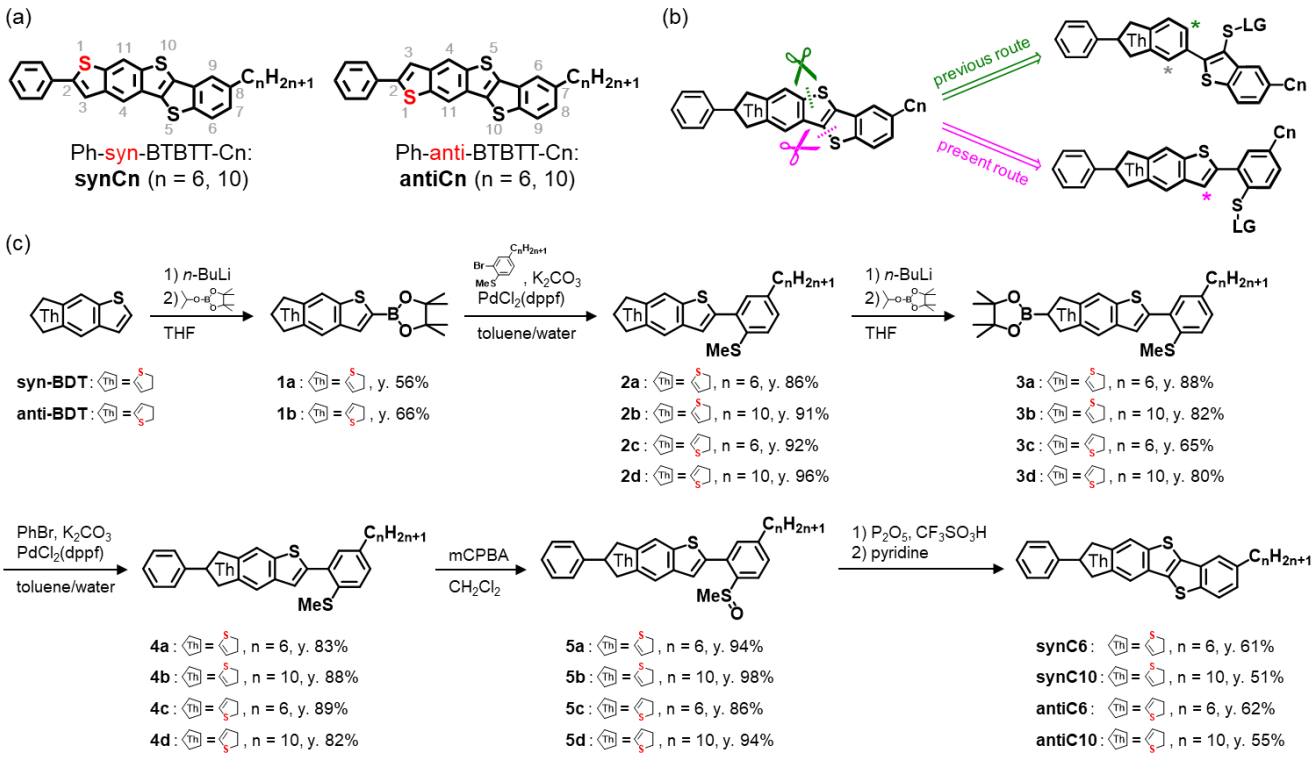

Scheme 1 (a) Chemical structures of syn-/anti-isomers of Ph-BTBTT-Cn. (b) Synthetic strategy for Ph-BTBTT-Cn derivatives employing a thiophene ring formation reaction. Previously reported route (green) and newly proposed route (purple) using the benzothiophene-/benzodithiophene-involved precursor, respectively. Note that the former precursor has two possible reaction sites including an undesirable position marked with gray asterisk affording isomeric byproducts. (c) Synthetic scheme of syn-/anti-isomers of Ph-BTBTT-Cn.

reaction sites on the phenyl-substituted benzothiophene unit. To avoid it, we employed another precursor comprising the benzodithiophene unit, which allows to afford syn-/anti-BTBTT skeletons selectively and efficiently.

According to the improved route as depicted in Scheme 1(c), we carried out the synthesis of a series of the BTBTT-isomers (**synCn** and **antiCn**). Using syn-/anti-isomers of benzodithiophene (BDT) as starting materials, we formed unsymmetric skeletons (**4**) by introducing an alkyl chain unit and a phenyl group in a step-by-step fashion though the lithiation/borylation reactions and the Suzuki−Miyaura cross-coupling reactions. After the oxidation of **4**, the intramolecular cyclization of the precursors (**5**) formed the BTBTT backbone. The crude products were finally purified by vacuum sublimation to afford a white powder for **synCn** and a pale yellow powder for **antiCn**. The present synthetic route remarkably improves the yields at the final step from 20% to 50-60% because the unnecessary cyclization at the carbon, denoted by gray star, in Scheme 1(b) is avoided.[42] The total six steps were conducted in good overall yields of around 20%.

Solubility and thermal properties. All the BTBTT-isomers are sufficiently soluble for solution-based thin-film processing in some aromatic or chlorinated solvents at room temperature (Figure 1). The solubility almost doubles for the same isomer as the alkyl chain shortens from n = 10 to n = 6, and this trend well matches the results for other thienoacene OSCs.[8,31,32] In a comparison of the same alkyl chain lengths, **antiCn** shows approximately 60% less solubility than **synCn**. All the compounds show a high thermal stability of

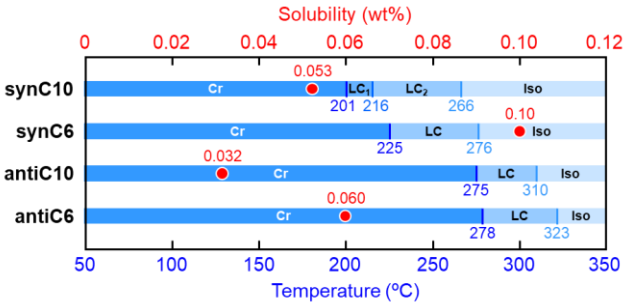

Figure 1 Solubility in chlorobenzene at 25 °C (red solid circle) and phase-transition behaviors (bluish bar) of the BTBTT-isomers.

the solid state up to at least 200 °C and have liquid crystalline (LC) phases, as shown by the thermogravimetry-differential thermal analysis (TG-DTA) in Figures 1 and S2. The temperatures of the crystal-LC and LC-isotropic phase transitions increase slightly with shortening the alkyl chain, and are much higher in **antiCn** than in **synCn**. The higher (lower) thermal stability of **antiCn** (**synCn**) is well consistent with the trend of the lower (higher) solubility, when we consider that these characteristics are determined by the crystal packing stability. The results also imply that the packing motif is distinct between **synCn** and **antiCn**.

Single-crystal growth and molecular packing. Figures 2(a)-(d) present micrographs of single crystals or recrystallized products from solutions for all the compounds. The crystal habits are clearly different between **synCn** and **antiCn**,

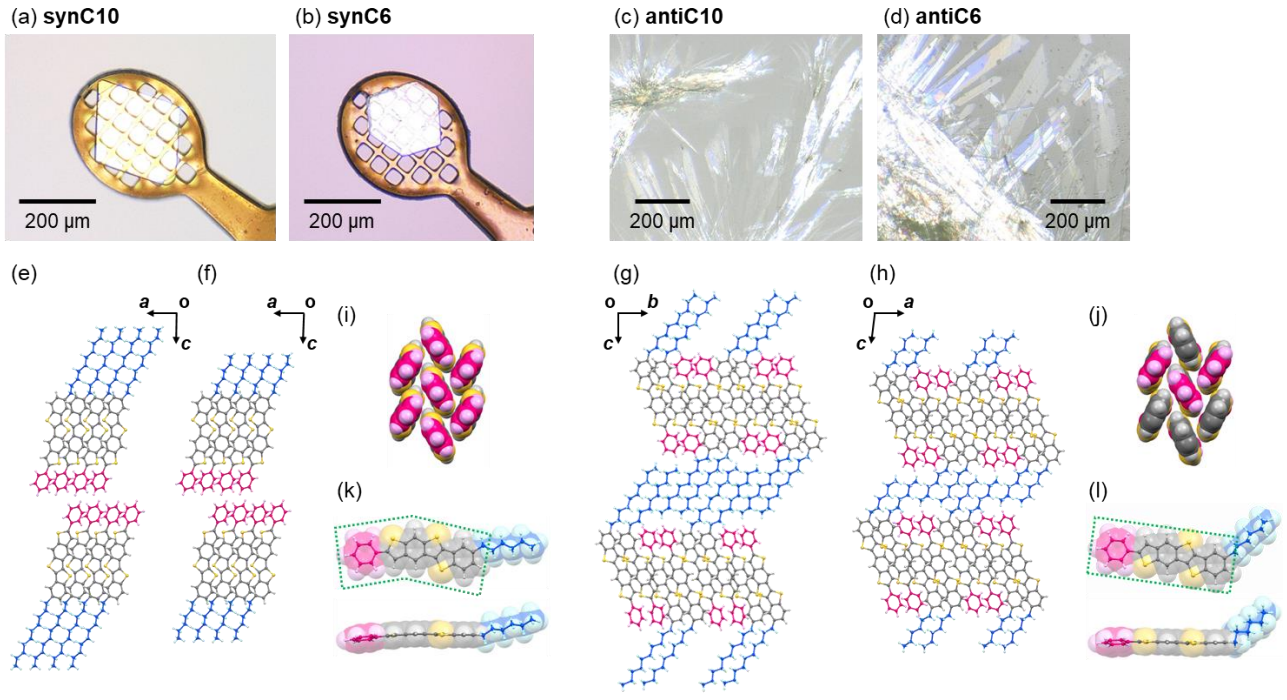

Figure 2 Optical images of the single crystals of (a) **synC10** and (b) **synC6** fixed on a mesh-type Litholoop and the crystalline solids of (c) **antiC10** and (d) **antiC6**. Experimental crystal structures projected along the intralayer direction for (e) **synC10**, (f) **synC6**, (g) **antiC10**, and (h) **antiC6**. Herringbone packings of (i) **synC6** and (j) **antiC6** (The hexyl chains are omitted for clarity.). Top and front views of one molecule of (k) **synC6** and (l) **antiC6** in the crystals. Green broken frame: approximate molecular shapes of the rigid π-conjugated skeleton composed of the phenyl ring and the BTBTT π-core.

but are independent of the alkyl chain length, as seen in the micrographs. The **synCn** affords plate-like single crystals suitable for X-ray diffraction analysis, whereas it is difficult to grow large and thick single crystals for **antiCn**; ultrathin flake-like crystals stacked to each other are mostly obtained, even under an optimized growth condition. Although sufficient x-ray diffraction intensity for structure analysis was not obtained from the **antiCn** crystal, the crystal structure of **antiCn** was successfully achieved by serial X-ray diffraction using free electron lasers (XFELs) and electron diffraction analyses. The resulting molecular packings are shown in Figures 2(e)-(j), and the crystallographic data are listed in Table S1. As expected, the molecular packing motifs are distinct between **synCn** and **antiCn**. The **synC6** forms a *b*-LHB packing being isomorphous to **synC10**,[42] while both **antiC6** and **antiC10** form unique *aai*-HB packing, in which the respective π-core layers are formed by a herringbone-type overlap arrangement between π-core moieties (*i.e.*, composed of BTBTT core and phenyl ring) of adjacent molecules aligned parallel and antiparallel to each other, whereas the alkyl-chain moieties are interdigitated with each other between the π-core layers. Despite these different layered structures, the herringbone angles (θ_{HB}) between the adjacent π-cores are almost the same for **synCn** and **antiCn** (Table S2). The notable variation of the molecular packing between **synCn** and **antiCn** should be clearly ascribed to the effect of isomeric change in BTBTT π-cores, the origin of which will be discussed in later section.

As seen from the crystal structures shown in Figures 2(k) and (l)), **synCn** and **antiCn** present particular difference in term of the whole molecular shape in the crystals. As for the rigid π-core moieties, **synCn** is composed of a slightly bent rod-like π-core, while **antiCn** has more linearly extended π-core. The feature is associated with the thiophene-fused isomeric effect on the shape of rigid π-core, and is responsible for the change of the molecular packing between **synCn** and **antiCn**, as discussed later. In contrast, the alkyl-chain orientation as to the π-core is also much different between **synCn** and **antiCn**; the alkyl chain is directed close to the molecular long axis in **synCn** with the bent angle of about 10°, while that is considerably bent of about 45° from the long axis of π-core in **antiCn** (Table S2). Both the alkyl conformations of **synCn** and **antiCn** are different from those of the geometry of isolated molecules optimized by DFT calculations (Table S2).

Here, we briefly describe the key results of the crystallographic analysis of **antiCn**. The general molecular arrangement is identical for **antiC6** and **antiC10**, but **antiC6** is more symmetric (space group $P2_1/c$) with two independent molecules in the unit cell (Z' = 2), while **antiC10** is less symmetric ($P1$) with Z' = 8. The neighboring molecules of **antiC6** are related by symmetry operations, but in the analysis of **antiC10**, these relationships are only pseudo-symmetric. By assuming that all molecules are independent with the space group $P1$, a model structure that better matches the diffraction data was finally achieved. The obtained structure shows slight differences in the molecular conformation among the eight independent molecules, in terms of the dihedral angles between the π-core and phenyl group/alkyl chain and the herringbone angles formed by the π-cores. Various aspects and origin of these features will be reported shortly.

Solution-processed crystalline thin films and their characteristics. Figure 3 summarizes results of drop-casting and blade-coating of the solutions of the compounds onto substrates; crossed-Nicols polarized micrographs are shown for the obtained thin films and products. The results of simple drop casting show a clear difference in the thin-film formability of the compounds; **synCn** produces uniform millimeter-scale thin films composed of single-crystalline domains that show clear brightness contrast in the images, while **antiCn** affords needle-like recrystallized products but not thin-film products. In contrast, the blade-coating technique allows to form millimeter-scale crystalline thin films for all compounds. However, the difference in the film-forming ability between **synCn** and **antiCn** is easily observed from the images; Fairly large single-crystalline domains are obtained for **synCn**, while **antiCn** affords elongated films composed of multiple domains that do not have clear boundaries to each other, where the extinction ratio in the crossed-Nicols image is not as clear as the **synCn** crystalline films, even after the film process conditions were fully optimized.

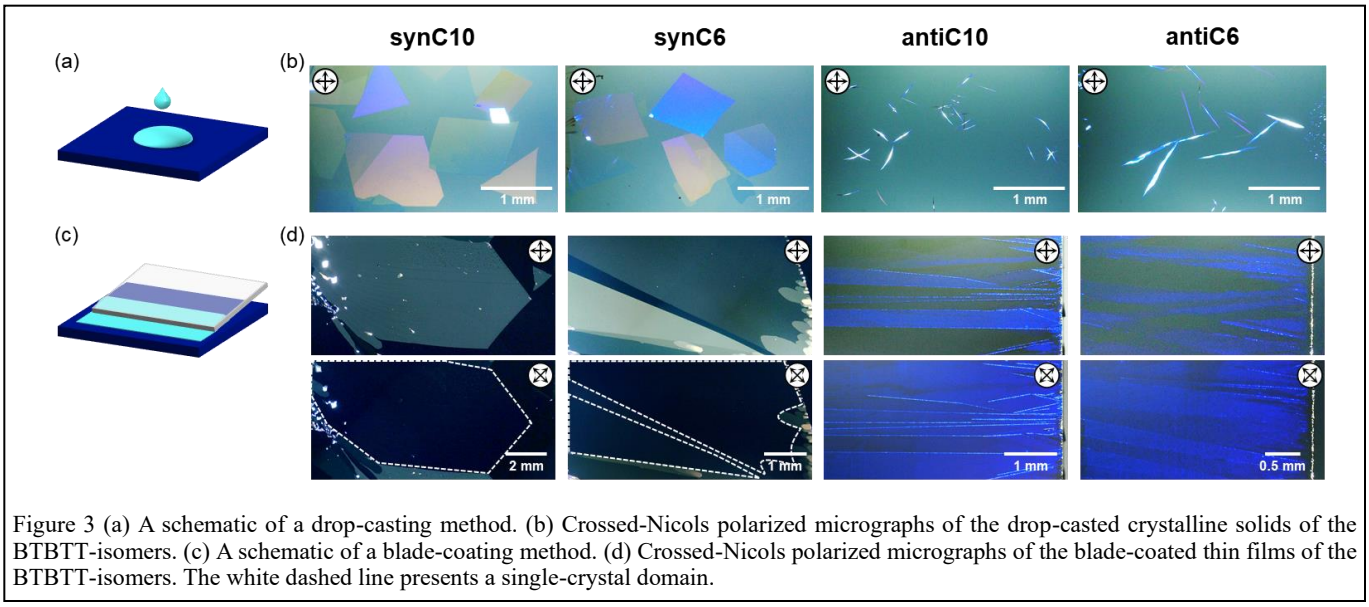

Figure 3 (a) A schematic of a drop-casting method. (b) Crossed-Nicols polarized micrographs of the drop-casted crystalline solids of the BTBTT-isomers. (c) A schematic of a blade-coating method. (d) Crossed-Nicols polarized micrographs of the blade-coated thin films of the BTBTT-isomers. The white dashed line presents a single-crystal domain.

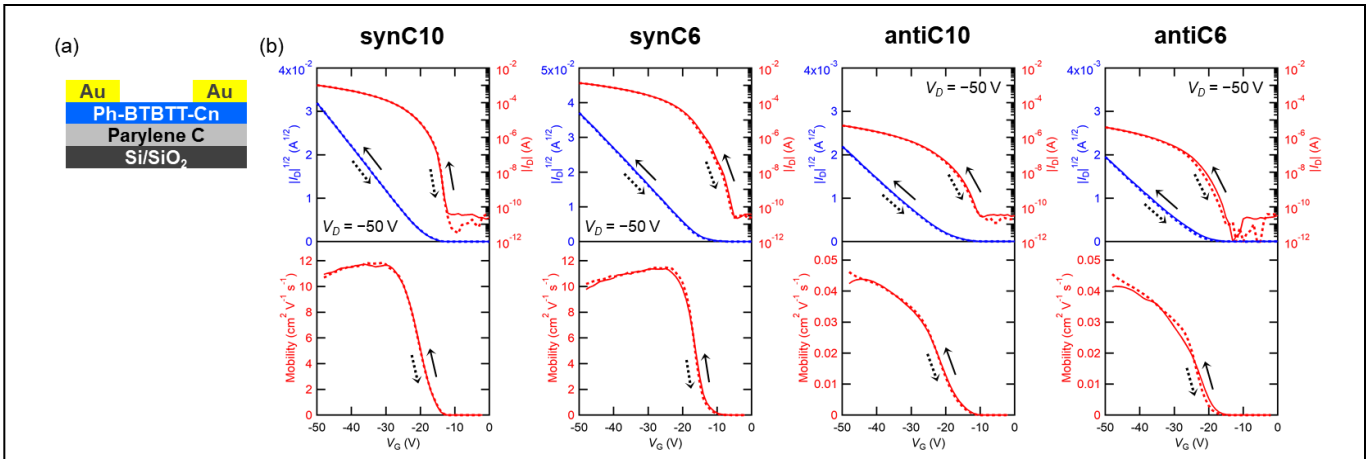

Figure 4 (a) A schematic of the BGTC-TFT device. (b) Transfer curves and the mobility plots in the saturation regions for the TFT devices based on the drop-casted thin films for syn-isomers and based on the blade-coated thin films for anti-isomers.

The crystalline states of both drop-casted and blade-coated films were examined by X-ray diffraction measurements (Figure S3). Clear Bragg reflections were observed in the **synCn** films; out-of-plane (00*l*) and single in-plane peak at 2θ of 18.09° for **synC6** and 18.18° for **synC10**, corresponding to the (020) diffractions (Figures S3(a) and (c)). The result indicates the crystal packing of the films with bulk crystals (Figure S3(e)). In contrast, a single weak out-of-plane diffraction is only observed for the **antiCn** films (Figures S3(b) and (d)), although no in-plane Bragg reflections were observed in the measurements. The *d*-spacing is estimated as about 25.2 Å for **antiC6** and 29.6 Å for **antiC10**, which are strictly different from the (002) reflections of bulk crystals (23.4 Å for **antiC6** and 27.7 Å for **antiC10**) but roughly corresponds to the length of linearly-extended molecules (23.8 Å for **antiC6** and 28.8 Å for **antiC10**). Atomic force microscopy (AFM) measurements reveal that the step height in the **antiC6** thin film is estimated to be about 2.4 nm that approximately corresponds to the single-molecular length of **antiC6** (Figure S4). We consider that the **antiCn** films should form smectic LC-like states, as schematically presented in Figure S3(f)),[71-76] and that the films do not have a long-range order suitable for XRD measurements. However, the details of the molecular arrangements in the films are not clear.

TFT characteristics. We fabricated bottom-gate, top-contact (BGTC)-type TFTs composed of an SiO_2 gate dielectric layer passivated by a parylene C layer, gold source-drain electrodes, and drop-casted films of **synCn** or blade-coated films of **antiCn** as channel layer (Figure 4(a)). Typical *p*-type characteristics are observed for all the compounds, as shown in Figures 4(b) and S5. All the TFTs show negligible hysteresis with almost the same threshold voltages of around –20 V. This indicates that the presence of carrier traps at the semiconductor/dielectric interface does not depend largely on the crystalline states of the OSC thin films.[77,78] In contrast, the carrier transport properties strongly depend on the

Table 1 Intermolecular interaction energies (E_{int}) for (a) **synC6** and (b) **antiC6**, between the central target molecule, shown exclusively by a space-filling model, and the neighboring molecules, shown by a ball and stick model, with interatomic distance shorter than 4 Å. The intermolecular contacts mostly between π-core moieties that form intralayer herringbone arrangements are defined as "Intralayer". In contrast, interlayer intermolecular contacts at the phenyl group and at the alkyl chain of the target molecule are defined as "Interlayer phenyl" and "Interlayer alkyl", respectively, where the latter involves interdigitated contacts between alkyl chains. The "Intralayer" contacts were decomposed into dispersion (E_{disp}), electrostatic (E_{es}), induction (E_{ind}), and short-range (E_{short}) interactions, by energy decomposition analysis. All energies were averaged for the crystallographically independent molecules.

(a) **synC6** (*b*-LHB)

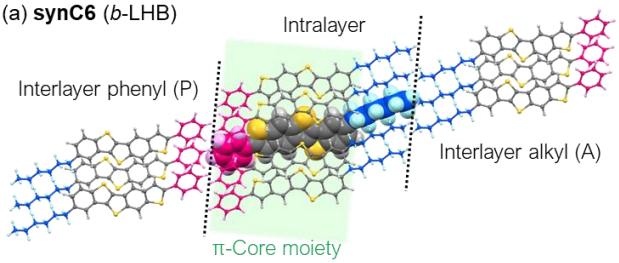

(b) **antiC6** (*aai*-HB)

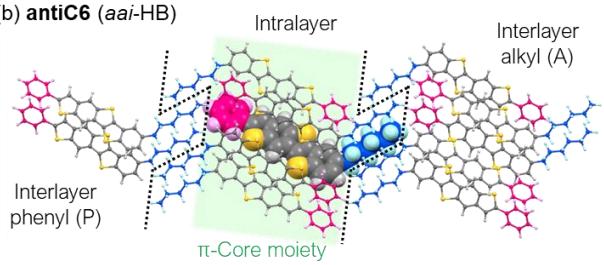

Molecule / Lattice (kcal/mol)		Whole molecule				π-Core moiety				
		Total	Intralayer	Interlayer-P	Interlayer-A	Intralayer				
		E_{int}	E_{int}	E_{int}	E_{int}	E_{int}	E_{disp}	E_{es}	E_{ind}	E_{short}
synC6	*b*-LHB	−105.25	−97.29	−5.04	−2.92	−77.99	−101.89	−6.01	−2.92	32.83
antiC6	*aai*-HB	−105.75	−91.86	−1.71	−12.18	−77.73	−103.19	−7.74	−3.13	36.33

isomeric BTBTT π-cores; **synCn** exhibit high saturation mobilities over 10 $cm^2 V^{-1} s^{-1}$ (average: 9.0 ± 1.5 $cm^2 V^{-1} s^{-1}$ for **synC10** and 8.7 ± 1.6 $cm^2 V^{-1} s^{-1}$ for **synC6**), while **antiCn** show relatively low mobilities (average: 0.041 ± 0.0036 $cm^2 V^{-1} s^{-1}$ for **antiC10** and 0.036 ± 0.0055 $cm^2 V^{-1} s^{-1}$ for **antiC6**). A similar tendency is observed in current on/off ratios: over 10^7 for **synCn** and around 10^5 for **antiCn**, respectively. These differences in carrier transport properties are closely related to the crystalline states of the OSC thin films.

Intermolecular interaction energies. To understand why the *b*-LHB and *aai*-HB lattices are formed with **synC6** and **antiC6**, respectively and selectively, we conducted dispersion-corrected density functional theory (DFT) calculations for intermolecular interactions using the optimized crystal structures of **synC6** and **antiC6**. The crystal structures were optimized starting from the structures obtained by the X-ray and electron diffraction measurements. The interaction energies were calculated for molecular pairs consisting of a molecule and its surrounding neighbors with the shortest interatomic distance of 4 Å or less.

Table 1 shows sum of interaction energy between molecules adjacent along inter- and intralayer directions, respectively. The total interaction energies are almost same between the different crystal lattices of **synC6** and **antiC6**. The intralayer interaction is dominant for both crystals, as they are composed of the rod-like OSC molecules. In contrast, the interlayer interaction becomes more important in *aai*-HB lattices of **antiC6** (−1.71 + −12.18 = −13.89 kcal/mol) than in *b*-LHB lattices of **synC6** (−5.04 + −2.92 = −7.96 kcal/mol), which can be clearly ascribed to the contribution of interdigitated contacts between alkyl chains. These features demonstrate the higher layered crystallinity in *b*-LHB lattices of **synC6** than in *aai*-HB lattices of **antiC6**. Interestingly, the interaction energy calculated only between the adjacent π-core moieties are al-

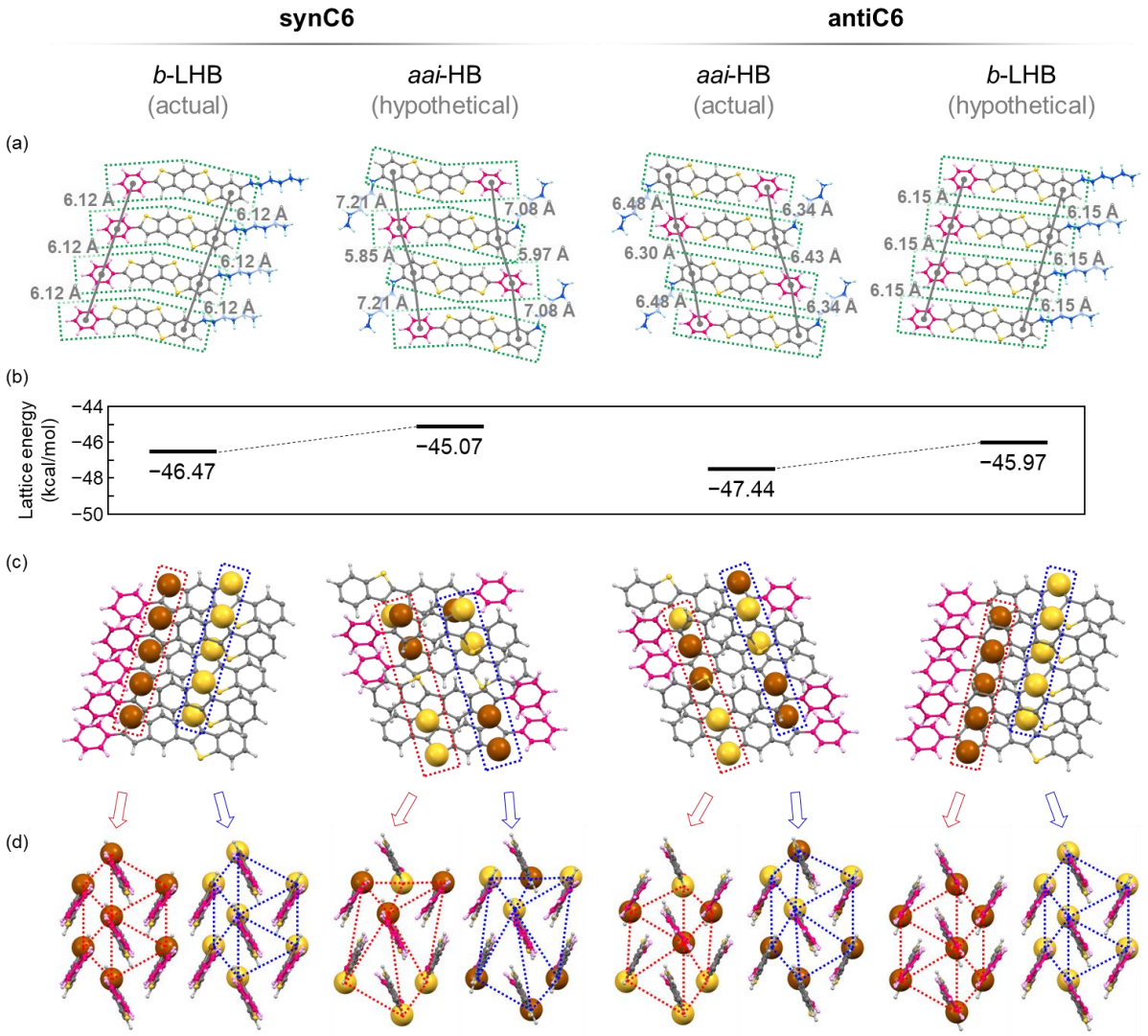

Figure 5 Molecular packing of the theoretically optimized crystal structures for **synC6** and **antiC6**. (a) Molecular arrangement in a slipped-parallel relationship. Green broken frame: approximate molecular shapes of the π-conjugated rigid skeleton composed of the phenyl ring and the BTBTT π-core. Gray solid line: intermolecular distances between the centroids of the adjacent benzene rings of the π-conjugated rigid skeleton, showing the uniformity of the molecular arrangements. (b) Lattice energy per one molecule. (c) Side and (d) front views of the herringbone packing of the π-skeleton. Red and blue broken lines: arrangement pattern of the adjacent sulfur atoms in the benzodithiophene unit highlighted by a space-filling model with yellow and brown color.

most same between the different crystal lattices (−77.99 kcal/mol in *b*-LHB lattices of **synC6** vs. −77.73 kcal/mol in *aai*-HB lattices of **antiC6**). The results imply that the *b*-LHB and *aai*-HB lattices are competitive in the syn- and anti-isomers, though it is not clear whether the distinct π-cores are suitable or not for the formation of parallel/antiparallel intralayer arrangements, respectively.

Origin of isomeric effect on distinct molecular packing. In the crystals formed by neutral molecules such as the OSCs used in the present study, attractive intermolecular forces are mainly derived from dispersion forces,[79,80] as is confirmed in Table 1. Repulsive force owing to the short-range orbital interaction should be balanced with the attractive forces, resulting in the formation of stable crystal packings.[81] Thus, larger lattice energy can be gained by closer intermolecular distance with keeping atom-atom distance larger than certain distances to avoid short-range repulsion. Conversely, crystal structures that involve larger void space between adjacent molecules becomes more unstable. The rule should be the basic origin why the different isomeric molecules afford distinct molecular packing.

Keeping the facts in mind, we investigated why the thiophene-fused isomers of **synC6** and **antiC6** form the *b*-LHB and *aai*-HB packings, respectively. For this purpose, we hypothetically generated the opposite types of packings (*aai*-HB lattice for **synC6** and the *b*-LHB lattice for **antiC6**), and compared their stability with that of actual crystals. Each hypothetical lattice is modeled by substituting **synC6** (**antiC6**) with **antiC6** (**synC6**) in the *b*-LHB (*aai*-HB) lattices, and then subjected the initial models to geometry optimizations (See the Experimental for details). The obtained molecular packing is presented in Figure 5(a), with the lattice parameters listed in Table S3 and the calculated powder patterns shown in Figure S6 (See Figure S7 for the transfer integrals and band structures calculated from these actual and hypothetical lattices). Based on the method which we call as "lattice-swapping approach", we found that the hypothetical packings for both isomers form slightly larger unit cell volume and are less stable than the actual packings, showing larger lattice energies of approximately 1.5 kcal/mol, as depicted in Figure 5(b). The calculated results are quite consistent with the actual packings for **synC6** and **antiC6**.

Based on the findings, we discuss the stabilities of actual and hypothetical packings in terms of the slightly different geometry of rigid π-conjugated skeletons that should affect the formation of close intralayer intermolecular packing or the opening between adjacent molecules. We first focus on the relatively bulky sulfur atoms and compare the arrangement patterns in the HB packing, as presented in Figures 5(c) and (d). The sulfur atoms are arranged in a slightly distorted hexagonal manner in the actual lattices, whereas they are unevenly arranged in the hypothetical *aai*-HB lattice of **synC6**. The latter feature should be unfavorable for close intermolecular packing. We also examined slipped-parallel arrangement in the HB packing as shown in Figure 5(a). It is found that the π-core of **synC6** is slightly bent and thus not suitable for close and uniform antiparallel molecular arrangement in the hypothetical *aai*-HB lattice. Finally, we investigated the intermolecular C−H···π distance in the *T*-shaped arrangements (Figure 6 and Table S4), as the fundamental unit for the HB packing.[82,83] We found that the H···π distances between the C-H terminals and the contacting π-electron plane are mostly shorter in the actual lattice than in the hypothetical lattice for both the isomers. These results corroborate that the actual lattices should be selectively formed by the tighter HB packing.

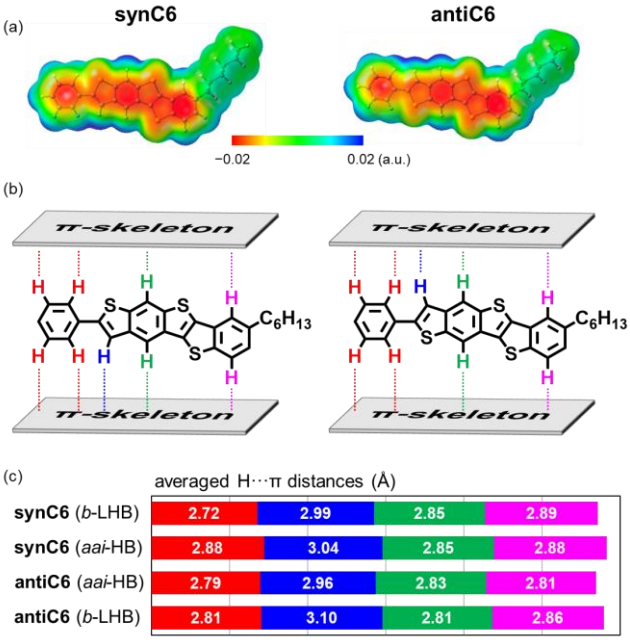

Figure 6 (a) Electrostatic potentials calculated for **synC6** and **antiC6** from B3LYP/6-311G** wave functions. (b) Schematics of intermolecular C−H···π interactions in the *T*-shaped arrangement. (c) Averaged distances of the H···π contacts.

CONCLUSION

We successfully synthesized two pairs of syn-/anti-isomers of **synCn** and **antiCn** with different alkyl chain lengths (n = 6, 10), and investigated the effect of unsymmetric thienoacenes involving different thiophene-fused isomers on the crystal packings and solid-state characteristics. All the compounds show sufficient solvent solubility for solution processing at room temperature and high thermal stability of the solid state up to 200 °C. These structural isomers afford distinct types of packing motifs, irrespective of the alkyl chain lengths: The **synCn** crystallizes into the *b*-LHB packing composed of *head-to-head* arrangement of unidirectionally-aligned monomolecular layers, while the **antiCn** forms *aai*-HB packing composed of alternating antiparallel alignment of π-cores and the alkyl chains are interdigitated with each other between the adjacent π-core layers. The observed packing difference is clearly associated with the film-forming ability and the TFT properties: The **synCn** easily forms a single-crystalline films that exhibit high carrier mobility over 10 $cm^2\ V^{-1}\ s^{-1}$, while the **antiCn** shows poor film-forming ability and moderate mobility. By comparing with hypothetical optimized structure models, we found that the isomeric effect on the distinct nature of molecular packing originates from the slightly different geometry of rigid π-conjugated skeleton that affects the formation of close intralayer intermolecular packing or the opening between adjacent molecules. We believe that these find-

ings will open further potential for crystal engineering in functional OSCs based on unsymmetric π-cores.

EXPERIMENTAL SECTION

Materials. Details of syntheses and characterizations for the title compounds, **synCn** and **antiCn**, is summarized in the Supporting Information.

Thermal Properties. Thermal properties were investigated by thermogravimetry-differential thermal analysis (TG-DTA; STA7200RV, Hitachi High-Tech Science Co.). TG-DTA measurements were performed in the range between room temperature and 500 °C at a heating rate of 5 K min^{-1} under N_2 atmosphere.

Crystal Growth. Plate-like single crystals of **synCn** suitable for X-ray diffraction were obtained by recrystallization from anisole solutions under ambient conditions. One crystal was collected from the solution using mesh-type LithoLoops (Molecular Dimensions Ltd.). Flake-like ultrathin single crystals of **antiCn** suitable for electron diffraction were obtained by recrystallization from mixed solutions of chlorobenzene and anisole (1:2 v/v).

X-ray Crystal Structure Analysis. X-ray crystallography was carried out for **synC6**. The single-crystal X-ray diffraction data were collected using a Rigaku AFC10 four-circle diffractometer equipped with a Pilatus 200 K hybrid pixel detector and a graphite monochromated Mo Kα radiation source (λ = 0.71073 Å). Data reduction with empirical absorption correction was performed using the CrysAlisPro software package.[84] The structure was solved by direct methods using the SHELXT program[85] and was refined by the full-matrix least-squares method using SHELXL[86] by applying anisotropic temperature factors for all nonhydrogen atoms. The hydrogen atoms were placed at geometrically calculated positions. All calculations were carried out by using the crystallographic software package Olex2-1.2.[87]

Serial XFEL Crystal Structure Analysis. XFEL crystallography[88] was carried out for serial crystal structure analyses from ultrathin flake-like crystals of the compound **antiC6**. The flakes were suspended in low-viscosity liquid paraffin and spread over a polyimide plate with an area of 4 x 4 mm^2. The XFEL measurement was performed at Beamline 3, SACLA XFEL facility[89]. The photon energy of the XFEL and the beam size were adjusted to 15.0 keV and ~1 μm, respectively. The sample plate was scanned over the entire plate with XZ-translation and phi-rotation movements, being exposed every 10 μm by XFEL pulses. The diffraction patterns were recorded on an MX300-HS detector (Rayonix) placed 90 mm downward from the sample plane. All data collection was performed at room temperature. Total 182,878 images were collected. The reference cell parameters, monoclinic, a = 13 Å, b = 7.8 Å, c = 47 Å, β = 97°, were obtained from rotational electron diffraction (see the next **Electron Crystal Structure Analysis** section) and provided for processing the serial diffraction images with CrystFEL suite.[90] 6,308 images (3.4% of the total collected images) were successfully indexed from extracted 24,253 images (13.3%) showing diffraction spots. The integrated and merged diffraction intensities were then used for ab initio phasing with SHELXT[85], and the initial structure was refined with SHELXL[86]. The data were tested for twinning using PLATON[91] and revealed the twin operator (-1 0 0/0 -1 0/0.8 0 1), which was included in the refinement. The bond geometry was restrained using the values from the structure of **synC10**. All non-hydrogen atoms were modeled with anisotropic displacement parameters and hydrogen atoms were generated using a riding model. The crystallographic parameters are summarized in Table S1.

Electron Crystal Structure Analysis. Electron crystallography was carried out[92] for crystal structure analyses from ultrathin flake-like crystals of the compounds **antiCn** at n = 6 and n = 10. The crystals obtained by drying up the anisole solution of **antiCn** were spread with Novec7100 (3M) or anisole onto a holey carbon film-coated TEM grid. The crystals were examined with a CRYO ARM 300 microscope (JEOL Ltd., Japan) operated at an accelerating voltage of 300 kV. Diffraction patterns were recorded on a DE-64 detector (Direct Electron, USA). Sequential frames were collected per crystal under parallel illumination by continuously rotating the sample stage from -68° to 68° at a rotation speed of 1 °/s. Total 96 and 67 rotational series, respectively for **antiC6** and **10**, were collected at cryogenic temperature (~93 K) using SerialEM and ParallEM[93,94]. Diffraction data were then processed with DIALS[95]. For **antiC6**, the common lattice parameters found in the rotation series were referred in **Serial XFEL Crystal Structure Analysis**. For **antiC10**, the initial phase was obtained by molecular replacement[96] using a part of the structure, as the direct method failed to yield reasonable solutions. The atomic model was manually adjusted and refined. The crystallographic parameters are included in Table S1.

Thin-Film Processing. To obtain thin films of **synCn** and **antiCn**, a drop-casting and blade-coating technique were employed. A heavily p-doped Si wafer covered with a 100 nm thermally grown SiO_2 dielectric layer was used as a substrate after being cleaned by sequential sonication in deionized water, acetone, 2-propyl alcohol, and deionized water. On the Si/SiO_2 (100 nm) wafer, a parylene C layer was deposited by chemical vapor deposition using a PDS 2010 LABCOTER (Specialty Coating Systems, USA) and DPX-C (di-chloro-di-p-xylylene) as a starting material. The thickness of the parylene C layer was evaluated to be around 40 nm. Solution-processes were done on the parylene C layer. Drop-casting was performed under a simple sealed atmosphere at room temperature using 0.02 wt% anisole (FUJIFILM Wako Pure Chemical Industries Ltd, 99.0%) solutions of **synCn** and 0.02 wt% chlorobenzene (Sigma-Aldrich, 99.9%) solutions of **antiCn**. A thin glass plate coated with Cytop (CTL-809 M; AGC Inc., Japan) was used as the coating blade, and its motion was controlled using a stepping motor (SHOT-302GS; Sigma Koki Co., Ltd., Japan). Blade-coating was performed using 0.02 wt% chlorobenzene solutions of **synCn** and **antiCn** at a sweep rate of 0.5 μm s^{-1} under ambient conditions for **synCn** and 7.5 μm s^{-1} under 60 °C for **antiCn**.

Thin-Film Properties. XRD measurements of the solution-processed thin films were carried out using a thin-film diffractometer (SOR-SmartLab; Rigaku Co., Ltd.), combined with monochromatized synchrotron X-ray radiation of an energy of 10 keV (1.238 Å) at the beamlines BL-7C of Photon Factory (PF), High-Energy Accelerator Research Organization (KEK). Atomic force microscopy (AFM) images of the thin films were recorded on a commercial AFM system (Dimen-

sion Edge, Bruker Co., Ltd.) in a tapping mode under ambient conditions.

Fabrication of TFTs. Gold source/drain electrodes were patterned on the **synCn** and **antiCn** thin films by thermal deposition using a shadow mask; the channel length and width of the devices, used for measurements of TFT characteristics, were 50 and 340 μm for **synC10**, 100 and 765 μm for **synC6**, and 50 and 500 μm for **antiCn**, respectively. The total capacitance of the gate dielectric composed of the SiO_2 and parylene C layers was estimated at approximately 26 nF cm^{-2}. For proper mobility evaluation, parts of the thin films outside (and between) the channels were trimmed using a homemade micromanipulator. The two-probe characteristics of the bottom-gate top-contact TFTs were measured under a N_2 atmosphere using a High-Power Source/Monitor Unit Module (E5280A; Keysight Technologies). The saturation mobility (μ_{sat}) was calculated from the following equation: $I_D = (W/2L)C_i\mu_{sat}(V_G-V_{th})^2$, where I_D is the drain current, W is the channel width, L is the channel length, C_i is the capacitance per unit area of the gate dielectric layer, and V_G and V_{th} are the gate and threshold voltage, respectively.

Computational Methods. The Quantum ESSPRESSO program[97,98] was used to optimize the crystal structures and calculations of lattice energies. The PBE functional[99] and Grimme's D3 dispersion correction[100] were used for the DFT calculations. The cutoff energies of plane wave basis set and charge density were 49 Ry and 441 Ry, respectively. The atomic positions and cell parameters were optimized in the optimizations of crystal structures. The lattice energies ($E_{lattice}$) were obtained according to the following equation, $E_{lattice} = E_{cryst} - N\,E_{mono}$, where E_{cryst} is the energy of the unit cell of crystal after geometry optimization, which contains N molecules, and E_{mono} is the energy of the optimized isolated molecule. Each molecule was isolated by the cubic unit cell with the edge of 35 Å in the geometry optimization. The hypothetical *b*-LHB lattice of **synC6** and *aai*-HB lattice of **antiC6** were generated through the following procedure: The atomic coordinates obtained from the diffraction experiments were partially modified using GaussView software,[101] converting the molecules from **synC6** (**antiC6**) to **antiC6** (**synC6**), whose modified coordinates were used as initial models for the optimizations of crystal structures.

Intermolecular interaction energies (E_{int}) between neighboring molecules were calculated at the B3LYP/6–311G** level[102] with Grimme's D3 dispersion correction using the Gaussian16 program,[103] based on the optimized crystal geometries. The basis set superposition error (BSSE)[104] was corrected by the counterpoise method.[105] The interaction energies between the π-conjugated skeletons composed of the phenyl group and the BTBTT core were calculated using the fragment structures in the crystals. The dangling bonds of the fragments were capped by hydrogen atoms in the calculations.

The intermolecular interaction energy was categorized into the contributions of dispersion force (E_{disp}), the electrostatic force (E_{es}), the induction force (E_{ind}), and short-range orbital-orbital interation (E_{short}). The E_{es} and E_{ind} were calculated using the ORIENT version 3.2.[106] E_{es} was calculated as the interactions between distributed multipoles[107] of interacting molecules using the ORIENT version 3.2. Distributed multipoles up to hexadecapole on all atoms were obtained from B3LYP/6-311G** level wave functions of isolated molecules using the GDMA program.[108] The E_{ind} was calculated as interactions of polarizable sites with the electric field produced by the distributed multipoles of monomers.[109] The atomic polarizabilities of carbon (a = 10 au) and sulfur (a = 20 au) were used for the calculations.[110] Distributed multipoles were used only to estimate the E_{es} and E_{ind}. The interaction energy calculated without the dispersion correction (E_{b3lyp}) is approximately the sum of the E_{es}, E_{ind}, and E_{short}. Thus, the E_{short} was calculated according to the equation; $E_{short} = E_{b3lyp} - E_{es} - E_{ind}$. The E_{disp} was calculated as the difference between the calculated interaction energies with and without dispersion correction according to the equation; $E_{disp} = E_{int} - E_{b3lyp}$.

Reorganization energies of the neutral molecules under positive charging were calculated with the four points method,[111,112] using the Gaussian16 program at the B3LYP/6-311G** level.

Transfer integrals between neighboring molecules were calculated for **synC6** and **antiC6** using the Gaussian16 program at the PW91/TZVP level using the HOMO generated from the theoretically optimized crystal geometries. The transfer integral t_{AB} between the molecular orbitals $|A\rangle$ and $|B\rangle$ was calculated by using the following equation:

$$t_{AB} = \frac{\langle A|F|B\rangle - \frac{1}{2}(\langle A|F|A\rangle + \langle B|F|B\rangle)\langle A|S|B\rangle}{1 - \langle A|S|B\rangle^2}$$

where F is the Fock matrix and S is the overlap matrix.

Electronic structures of **synC6** and **antiC6** were calculated at the PBE level of theory[99] using the plane wave basis set and pseudopotentials as implemented in the Quantum Espresso program.[97,98] The self-consistent calculations are computed with the cutoff energy of 25 Ry for plane wave and 225 Ry for charge density, respectively, and the Brillouin-zone integrations of a 3 × 3 × 1 k-points mesh.

ASSOCIATED CONTENT

The Supporting Information is available free of charge on the ACS Publications website at DOI:

Synthetic procedures and characterization data, thermogravimetry-differential thermal analysis (TG-DTA), crystallographic data obtained from the diffraction measurements and obtained through the theoretical optimization, molecular conformation analysis, and thin-film characterizations.

Crystallographic data for **synC6** (CIF)

Crystallographic data for **antiC6** (CIF)

Crystallographic data for **antiC10** (CIF)

AUTHOR INFORMATION

Corresponding Author

* E-mail: t-higashino@aist.go.jp

ORCID

Toshiki Higashino: 0000-0002-9227-8207

Satoru Inoue: 0000-0002-1943-1594

Shunto Arai: 0000-0002-0055-3006

Seiji Tsuzuki: 0000-0001-8518-0300

Hiroyuki Matsui: 0000-0003-1956-9603
Reiji Kumai: 0000-0002-5320-0028
Kiyofumi Takaba: 0000-0002-2927-0608
Saori Maki-Yonekura: 0000-0002-8295-8794
Hirofumi Kurokawa: 0000-0002-1144-3400
Kensuke Tono: 0000-0003-1218-3759
Koji Yonekura: 0000-0001-5520-4391
Tatsuo Hasegawa:0000-0001-5187-7483

Notes

The authors declare no competing financial interest.

ACKNOWLEDGMENT

This study was partly supported by JSPS KAKENHI Grant Numbers 20H05867, 21K14699, 21H04651, and 18K19161, JST CREST Grant Number JPMJCR18J2, and JST-Mirai Program (Grant Number JPMJMI20G5). The XFEL experiments were performed at the BL3 of SACLA with the approval of the Japan Synchrotron Radiation Research Institute (JASRI) (Proposal No. 2021B8018). Synchrotron radiation experiments were performed under the approval of the Photon Factory Program Advisory Committee (Proposal No. 2020S2-001).

REFERENCES

(1) Takimiya, K.; Shinamura, S.; Osaka, I.; Miyazaki, E. Thienoacene-Based Organic Semiconductors. *Adv. Mater.* **2011**, *23*, 4347–4370.
(2) Wang, C.; Dong, H.; Hu, W.; Liu, Y.; Zhu, D. Semiconducting π-Conjugated Systems in Field-Effect Transistors: A Material Odyssey of Organic Electronics. *Chem. Rev.* **2012**, *112*, 2208–2267.
(3) Mei, J.; Diao, Y.; Appleton, A. L.; Fang, L.; Bao, Z. Integrated Materials Design of Organic Semiconductors for Field-Effect Transistors. *J. Am. Chem. Soc.* **2013**, *135*, 6724–6746.
(4) Okamoto, T.; Yu, C. P.; Mitsui, C.; Yamagishi, M.; Ishii, H.; Takeya, J. Bent-Shaped p-Type Small-Molecule Organic Semiconductors: A Molecular Design Strategy for Next-Generation Practical Applications. *J. Am. Chem. Soc.* **2020**, *142*, 9083–9096.
(5) Dong, H.; Fu, X.; Liu, J.; Wang, Z.; Hu, W. 25th Anniversary Article: Key Points for High-Mobility Organic Field-Effect Transistors. *Adv. Mater.* **2013**, *25*, 6158–6183.
(6) Fratini, S.; Ciuchi, S.; Mayou, D.; de Laissardière, G. T.; Troisi, A. A Map of High-Mobility Molecular Semiconductors. *Nat. Mater.* **2017**, *16*, 998–1002.
(7) Park, S. K.; Kim, J. H.; Park, S. Y. Organic 2D Optoelectronic Crystals: Charge Transport, Emerging Functions, and Their Design Perspective. *Adv. Mater.* **2018**, *30*, 1704759.
(8) Ebata, H.; Izawa, T.; Miyazaki, E.; Takimiya, K.; Ikeda, M.; Kuwabara, H.; Yui, T. Highly Soluble [1]Benzothieno[3,2-*b*]Benzothiophene (BTBT) Derivatives for High-Performance, Solution-Processed Organic Field-Effect Transistors. *J. Am. Chem. Soc.* **2007**, *129*, 15732–15733.
(9) Gao, P.; Beckmann, D.; Tsao, H. N.; Feng, X.; Enkelmann, V.; Baumgarten, M.; Pisula, W.; Müllen, K. Dithieno[2,3-*d*;2′,3′-*d*′]Benzo[1,2-*b*;4,5-*b*′]Dithiophene (DTBDT) as Semiconductor for High-Performance, Solution-Processed Organic Field-Effect Transistors. *Adv. Mater.* **2009**, *21*, 213–216.
(10) Minemawari, H.; Yamada, T.; Matsui, H.; Tsutsumi, J.; Haas, S.; Chiba, R.; Kumai, R.; Hasegawa, T. Inkjet Printing of Single-Crystal Films. *Nature* **2011**, *475*, 364–367.
(11) Okamoto, T.; Mitsui, C.; Yamagishi, M.; Nakahara, K.; Soeda, J.; Hirose, Y.; Miwa, K.; Sato, H.; Yamano, A.; Matsushita, T.; Uemura, T.; Takeya, J. V-Shaped Organic Semiconductors With Solution Processability, High Mobility, and High Thermal Durability. *Adv. Mater.* **2013**, *25*, 6392–6397.
(12) Yuan, Y.; Giri, G.; Ayzner, A. L.; Zoombelt, A. P.; Mannsfeld, S. C. B.; Chen, J.; Nordlund, D.; Toney, M. F.; Huang, J.; Bao, Z. Ultra-High Mobility Transparent Organic Thin Film Transistors Grown by an off-Centre Spin-Coating Method. *Nat. Commun.* **2014**, *5*, 3005.
(13) Mitsui, C.; Okamoto, T.; Yamagishi, M.; Tsurumi, J.; Yoshimoto, K.; Nakahara, K.; Soeda, J.; Hirose, Y.; Sato, H.; Yamano, A.; Uemura, T.; Takeya, J. High-Performance Solution-Processable N-Shaped Organic Semiconducting Materials with Stabilized Crystal Phase. *Adv. Mater.* **2014**, *26*, 4546–4551.
(14) Cho, J.-M.; Higashino, T.; Mori, T. Band-like Transport down to 20 K in Organic Single-Crystal Transistors Based on Dioctylbenzothienobenzothiophene. *Appl. Phys. Lett.* **2015**, *106*, 193303.
(15) Peng, B.; Huang, S.; Zhou, Z.; Chan, P. K. L. Solution-Processed Monolayer Organic Crystals for High-Performance Field-Effect Transistors and Ultrasensitive Gas Sensors. *Adv. Funct. Mater.* **2017**, *27*, 1700999.
(16) Ogawa, Y.; Yamamoto, K.; Miura, C.; Tamura, S.; Saito, M.; Mamada, M.; Kumaki, D.; Tokito, S.; Katagiri, H. Asymmetric Alkylthienyl Thienoacenes Derived from Anthra[2,3-*b*]Thieno[2,3-*d*]Thiophene for Solution-Processable Organic Semiconductors. *ACS Appl. Mater. Interfaces* **2017**, *9*, 9902–9909.
(17) Mitsui, C.; Tsuyama, H.; Shikata, R.; Murata, Y.; Kuniyasu, H.; Yamagishi, M.; Ishii, H.; Yamamoto, A.; Hirose, Y.; Yano, M.; Takehara, T.; Suzuki, T.; Sato, H.; Yamano, A.; Fukuzaki, E.; Watanabe, T.; Usami, Y.; Takeya, J.; Okamoto, T. High Performance Solution-Crystallized Thin-Film Transistors Based on V-Shaped Thieno[3,2-*f*:4,5-*f*′]Bis[1]Benzothiophene Semiconductors. *J. Mater. Chem. C* **2017**, *5*, 1903–1909.
(18) Yamaguchi, Y.; Kojiguchi, Y.; Kawata, S.; Mori, T.; Okamoto, K.; Tsutsui, M.; Koganezawa, T.; Katagiri, H.; Yasuda, T. Solution-Processable Organic Semiconductors Featuring S-Shaped Dinaphthothienothiophene (S-DNTT): Effects of Alkyl Chain Length on Self-Organization and Carrier Transport Properties. *Chem. Mater.* **2020**, *32*, 5350–5360.
(19) Han, M. J.; Lee, D.-W.; Lee, E. K.; Kim, J.-Y.; Jung, J. Y.; Kang, H.; Ahn, H.; Shin, T. J.; Yoon, D. K.; Park, J.-I. Molecular Orientation Control of Liquid Crystal Organic Semiconductor for High-Performance Organic Field-Effect Transistors. *ACS Appl. Mater. Interfaces* **2021**, *13*, 11125–11133.
(20) Matsunaga, A.; Ogawa, Y.; Kumaki, D.; Tokito, S.; Katagiri, H. Control of Molecular Orientation in Organic Semiconductors Using Weak Iodine–Iodine Interactions. *J. Phys. Chem. Lett.* **2021**, *12*, 111–116.
(21) Yu, C. P.; Kumagai, S.; Kushida, T.; Mitani, M.; Mitsui, C.; Ishii, H.; Takeya, J.; Okamoto, T. Mixed-Orbital Charge Transport in N-Shaped Benzene- and Pyrazine-Fused Organic Semiconductors. *J. Am. Chem. Soc.* **2022**, *144*, 11159–11167.
(22) Higashino, T.; Akiyama, Y.; Kojima, H.; Kawamoto, T.; Mori, T. Organic Semiconductors and Conductors with Tert-Butyl Substituents. *Crystals* **2012**, *2*, 1222–1238.
(23) Vyas, V. S.; Gutzler, R.; Nuss, J.; Kern, K.; Lotsch, B. V. Optical Gap in Herringbone and π-Stacked Crystals of [1]Benzothieno[3,2-*b*]Benzothiophene and Its Brominated Derivative. *CrystEngComm* **2014**, *16*, 7389–7392.
(24) Tsutsui, Y.; Schweicher, G.; Chattopadhyay, B.; Sakurai, T.; Arlin, J.-B. B.; Ruzié, C.; Aliev, A.; Ciesielski, A.; Colella, S.; Kennedy, A. R.; Lemaur, V.; Olivier, Y.; Hadji, R.; Sanguinet, L.; Castet, F.; Osella, S.; Dudenko, D.; Beljonne, D.; Cornil, J.; Samorì, P.; Seki, S.; Geerts, Y. H. Unraveling Unprecedented Charge Carrier Mobility through Structure Property Relationship of Four Isomers of Didodecyl[1]Benzothieno[3,2-*b*][1]Benzothiophene. *Adv. Mater.* **2016**, *28*, 7106–7114.
(25) Higashino, T.; Dogishi, M.; Kadoya, T.; Sato, R.; Kawamoto, T.; Mori, T. Air-Stable n-Channel Organic Field-Effect Transistors Based on Charge-Transfer Complexes Including Dimethoxybenzothienobenzothiophene and Tetracyanoquinodimethane Derivatives. *J. Mater. Chem. C* **2016**, *4*, 5981–5987.

(26) Klues, M.; Witte, G. Crystalline Packing in Pentacene-like Organic Semiconductors. *CrystEngComm* **2018**, *20*, 63–74.
(27) Mohankumar, M.; Chattopadhyay, B.; Hadji, R.; Sanguinet, L.; Kennedy, A. R.; Lemaur, V.; Cornil, J.; Fenwick, O.; Samorì, P.; Geerts, Y. Oxacycle-Fused [1]Benzothieno[3,2-*b*][1]Benzothiophene Derivatives: Synthesis, Electronic Structure, Electrochemical Properties, Ionisation Potential, and Crystal Structure. *Chempluschem* **2019**, *84*, 1263–1269.
(28) Higashino, T.; Ueda, A.; Mori, H. Di- and Tetramethoxy Benzothienobenzothiophenes: Substitution Position Effects on the Intermolecular Interactions, Crystal Packing and Transistor Properties. *New J. Chem.* **2019**, *43*, 884–892.
(29) Matsunaga, A.; Ogawa, Y.; Tamura, S.; Yamamoto, K.; Katagiri, H. Molecular Structure-Property Relationships of the Asymmetric Thienoacenes: Naphtho[2,3-*b*]Thieno[2,3-*d*]Thiophene, Anthra[2,3-*b*]Thieno[2,3-*d*]Thiophene, and Their Thienyl Derivatives. *ChemistrySelect* **2021**, *6*, 4506–4510.
(30) Iino, H.; Usui, T.; Hanna, J.-I. Liquid Crystals for Organic Thin-Film Transistors. *Nat. Commun.* **2015**, *6*, 6828.
(31) Inoue, S.; Minemawari, H.; Tsutsumi, J.; Chikamatsu, M.; Yamada, T.; Horiuchi, S.; Tanaka, M.; Kumai, R.; Yoneya, M.; Hasegawa, T. Effects of Substituted Alkyl Chain Length on Solution-Processable Layered Organic Semiconductor Crystals. *Chem. Mater.* **2015**, *27*, 3809–3812.
(32) Minemawari, H.; Tanaka, M.; Tsuzuki, S.; Inoue, S.; Yamada, T.; Kumai, R.; Shimoi, Y.; Hasegawa, T. Enhanced Layered-Herringbone Packing Due to Long Alkyl Chain Substitution in Solution-Processable Organic Semiconductors. *Chem. Mater.* **2017**, *29*, 1245–1254.
(33) Yoneya, M.; Minemawari, H.; Yamada, T.; Hasegawa, T. Interface-Mediated Self-Assembly in Inkjet Printing of Single-Crystal Organic Semiconductor Films. *J. Phys. Chem. C* **2017**, *121*, 8796–8803.
(34) Hamai, T.; Arai, S.; Minemawari, H.; Inoue, S.; Kumai, R.; Hasegawa, T. Tunneling and Origin of Large Access Resistance in Layered-Crystal Organic Transistors. *Phys. Rev. Appl.* **2017**, *8*, 054011.
(35) Arai, S.; Inoue, S.; Hamai, T.; Kumai, R.; Hasegawa, T. Semiconductive Single Molecular Bilayers Realized Using Geometrical Frustration. *Adv. Mater.* **2018**, *30*, 1707256.
(36) Inoue, S.; Shinamura, S.; Sadamitsu, Y.; Arai, S.; Horiuchi, S.; Yoneya, M.; Takimiya, K.; Hasegawa, T. Extended and Modulated Thienothiophenes for Thermally Durable and Solution-Processable Organic Semiconductors. *Chem. Mater.* **2018**, *30*, 5050–5060.
(37) Inoue, S.; Higashino, T.; Arai, S.; Kumai, R.; Matsui, H.; Tsuzuki, S.; Horiuchi, S.; Hasegawa, T. Regioisomeric Control of Layered Crystallinity in Solution-Processable Organic Semiconductors. *Chem. Sci.* **2020**, *11*, 12493–12505.
(38) Kitahara, G.; Inoue, S.; Higashino, T.; Ikawa, M.; Hayashi, T.; Matsuoka, S.; Arai, S.; Hasegawa, T. Meniscus-Controlled Printing of Single-Crystal Interfaces Showing Extremely Sharp Switching Transistor Operation. *Sci. Adv.* **2020**, *6*, eabc8847.
(39) Miyata, R.; Inoue, S.; Nakajima, K.; Hasegawa, T. Insulating Polymer Blend Organic Thin-Film Transistors Based on Bilayer-Type Alkylated Benzothieno[3,2-*b*]Naphtho[2,3-*b*]Thiophene. *ACS Appl. Mater. Interfaces* **2022**, *14*, 17719–17726.
(40) Higashino, T.; Inoue, S.; Sadamitsu, Y.; Arai, S.; Horiuchi, S.; Hasegawa, T. Bilayer-Type Layered Herringbone Packing in 3-*n*-Octyl-9-Phenyl-Benzothieno[3,2-*b*]Naphtho[2,3-*b*]Thiophene. *Chem. Lett.* **2019**, *48*, 453–456.
(41) Higashino, T.; Arai, S.; Inoue, S.; Tsuzuki, S.; Shimoi, Y.; Horiuchi, S.; Hasegawa, T.; Azumi, R. Architecting Layered Molecular Packing in Substituted Benzobisbenzothiophene (BBBT) Semiconductor Crystals. *CrystEngComm* **2020**, *22*, 3618–3626.
(42) Higashino, T.; Inoue, S.; Arai, S.; Matsui, H.; Toda, N.; Horiuchi, S.; Azumi, R.; Hasegawa, T. Architecting Layered Crystalline Organic Semiconductors Based on Unsymmetric π-Extended Thienoacenes. *Chem. Mater.* **2021**, *33*, 7379–7385.
(43) Laquindanum, J. G.; Katz, H. E.; Lovinger, A. J. Synthesis, Morphology, and Field-Effect Mobility of Anthradithiophenes. *J. Am. Chem. Soc.* **1998**, *120*, 664–672.
(44) Payne, M. M.; Odom, S. A.; Parkin, S. R.; Anthony, J. E. Stable, Crystalline Acenedithiophenes with up to Seven Linearly Fused Rings. *Org. Lett.* **2004**, *6*, 3325–3328.
(45) Payne, M. M.; Parkin, S. R.; Anthony, J. E.; Kuo, C.-C.; Jackson, T. N. Organic Field-Effect Transistors from Solution-Deposited Functionalized Acenes with Mobilities as High as 1 cm2/V·s. *J. Am. Chem. Soc.* **2005**, *127*, 4986–4987.
(46) Subramanian, S.; Park, S. K.; Parkin, S. R.; Podzorov, V.; Jackson, T. N.; Anthony, J. E. Chromophore Fluorination Enhances Crystallization and Stability of Soluble Anthradithiophene Semiconductors. *J. Am. Chem. Soc.* **2008**, *130*, 2706–2707.
(47) Jurchescu, O. D.; Subramanian, S.; Kline, R. J.; Hudson, S. D.; Anthony, J. E.; Jackson, T. N.; Gundlach, D. J. Organic Single-Crystal Field-Effect Transistors of a Soluble Anthradithiophene. *Chem. Mater.* **2008**, *20*, 6733–6737.
(48) Yamamoto, T.; Ogawa, S.; Sato, R. Selective Synthesis, Structure and Oxidation Properties of Isomeric 1,4-Dithiins Fused to Two Benzo[*b*]Thiophenes. *Tetrahedron Lett.* **2004**, *45*, 7943–7946.
(49) Wex, B.; Kaafarani, B. R.; Kirschbaum, K.; Neckers, D. C. Synthesis of the Anti and Syn Isomers of Thieno[*f,f*']Bis[1]Benzothiophene. Comparison of the Optical and Electrochemical Properties of the Anti and Syn Isomers. *J. Org. Chem.* **2005**, *70*, 4502–4505.
(50) Li, Z.; Lim, Y.-F.; Kim, J. B.; Parkin, S. R.; Loo, Y.-L.; Malliaras, G. G.; Anthony, J. E. Isomerically Pure Electron-Deficient Anthradithiophenes and Their Acceptor Performance in Polymer Solar Cells. *Chem. Commun.* **2011**, *47*, 7617.
(51) Tylleman, B.; Vande Velde, C. M. L.; Balandier, J.-Y.; Stas, S.; Sergeyev, S.; Geerts, Y. H. Synthesis of Isomerically Pure Anti-Anthradithiophene Derivatives. *Org. Lett.* **2011**, *13*, 5208–5211.
(52) Mamada, M.; Minamiki, T.; Katagiri, H.; Tokito, S. Synthesis, Physical Properties, and Field-Effect Mobility of Isomerically Pure Syn-/Anti-Anthradithiophene Derivatives. *Org. Lett.* **2012**, *14*, 4062–4065.
(53) Nakano, M.; Niimi, K.; Miyazaki, E.; Osaka, I.; Takimiya, K. Isomerically Pure Anthra[2,3-*b*:6,7-*b*′]-Difuran (Anti-ADF), -Dithiophene (Anti-ADT), and -Diselenophene (Anti-ADS): Selective Synthesis, Electronic Structures, and Application to Organic Field-Effect Transistors. *J. Org. Chem.* **2012**, *77*, 8099–8111.
(54) Chen, Y.-L.; Hsu, J.-Y.; Lin, F.-Y.; Lai, Y.-Y.; Chou, H.-C.; Cheng, Y.-J. Synthesis and Isomeric Effects of Ladder-Type Alkylated Terbenzodithiophene Derivatives. *J. Org. Chem.* **2016**, *81*, 2534–2542.
(55) Hallani, R. K.; Thorley, K. J.; Mei, Y.; Parkin, S. R.; Jurchescu, O. D.; Anthony, J. E. Structural and Electronic Properties of Crystalline, Isomerically Pure Anthradithiophene Derivatives. *Adv. Funct. Mater.* **2016**, *26*, 2341–2348.
(56) Diemer, P. J.; Hayes, J.; Welchman, E.; Hallani, R.; Pookpanratana, S. J.; Hacker, C. A.; Richter, C. A.; Anthony, J. E.; Thonhauser, T.; Jurchescu, O. D. The Influence of Isomer Purity on Trap States and Performance of Organic Thin-Film Transistors. *Adv. Electron. Mater.* **2017**, *3*, 1600294.
(57) Oyama, T.; Mori, T.; Hashimoto, T.; Kamiya, M.; Ichikawa, T.; Komiyama, H.; Yang, Y. S.; Yasuda, T. High-Mobility Regioisomeric Thieno[f,f']Bis[1]Benzothiophenes: Remarkable Effect of Syn / Anti Thiophene Configuration on Optoelectronic Properties, Self-Organization, and Charge-Transport Functions in Organic Transistors. *Adv. Electron. Mater.* **2018**, *4*, 1700390.
(58) Lehnherr, D.; Waterloo, A. R.; Goetz, K. P.; Payne, M. M.; Hampel, F.; Anthony, J. E.; Jurchescu, O. D.; Tykwinski, R. R. Isomerically Pure Syn-Anthradithiophenes: Synthesis, Properties, and FET Performance. *Org. Lett.* **2012**, *14*, 3660–3663.
(59) Mamada, M.; Katagiri, H.; Mizukami, M.; Honda, K.; Minamiki, T.; Teraoka, R.; Uemura, T.; Tokito, S. Syn-/Anti-Anthradithiophene

Derivative Isomer Effects on Semiconducting Properties. *ACS Appl. Mater. Interfaces* **2013**, *5*, 9670–9677.
(60) Hailey, A. K.; Petty, A. J.; Washbourne, J.; Thorley, K. J.; Parkin, S. R.; Anthony, J. E.; Loo, Y.-L. Understanding the Crystal Packing and Organic Thin-Film Transistor Performance in Isomeric Guest–Host Systems. *Adv. Mater.* **2017**, *29*, 1700048.
(61) Coropceanu, V.; Kwon, O.; Wex, B.; Kaafarani, B. R.; Gruhn, N. E.; Durivage, J. C.; Neckers, D. C.; Brédas, J.-L. Vibronic Coupling in Organic Semiconductors: The Case of Fused Polycyclic Benzene–Thiophene Structures. *Chem. - A Eur. J.* **2006**, *12*, 2073–2080.
(62) Yi, W.; Zhao, S.; Sun, H.; Kan, Y.; Shi, J.; Wan, S.; Li, C.; Wang, H. Isomers of Organic Semiconductors Based on Dithienothiophenes: The Effect of Sulphur Atoms Positions on the Intermolecular Interactions and Field-Effect Performances. *J. Mater. Chem. C* **2015**, *3*, 10856–10861.
(63) Chen, H.-Y.; Schweicher, G.; Planells, M.; Ryno, S. M.; Broch, K.; White, A. J. P.; Simatos, D.; Little, M.; Jellett, C.; Cryer, S. J.; Marks, A.; Hurhangee, M.; Brédas, J.-L.; Sirringhaus, H.; McCulloch, I. Crystal Engineering of Dibenzothiophenothieno[3,2-*b*]Thiophene (DBTTT) Isomers for Organic Field-Effect Transistors. *Chem. Mater.* **2018**, *30*, 7587–7592.
(64) Hu, P.; Ye, J.; Jiang, H. Which Isomer Is Better for Charge Transport: Anti- or Syn-? *J. Mater. Chem. C* **2019**, *7*, 5858–5873.
(65) Jiang, H.; Zhu, S.; Cui, Z.; Li, Z.; Liang, Y.; Zhu, J.; Hu, P.; Zhang, H.-L.; Hu, W. High-Performance Five-Ring-Fused Organic Semiconductors for Field-Effect Transistors. *Chem. Soc. Rev.* **2022**, *51*, 3071–3122.
(66) Kanazawa, K.; Bulgarevich, K.; Kawabata, K.; Takimiya, K. Uncovered Effects of Thieno[2,3-*b*]Thiophene Substructure in a Tetrathienoacene Backbone: Reorganization Energy and Intermolecular Interaction. *Chem. Mater.* **2023**, *35*, 280–288.
(67) He, K.; Zhou, S.; Li, W.; Tian, H.; Tang, Q.; Zhang, J.; Yan, D.; Geng, Y.; Wang, F. Five-Ring-Fused Asymmetric Thienoacenes for High Mobility Organic Thin-Film Transistors: The Influence of the Position of the S Atom in the Terminal Thiophene Ring. *J. Mater. Chem. C* **2019**, *7*, 3656–3664.
(68) Dong, Y.; Li, H.; Liu, J.; Zhang, J.; Shi, X.; Shi, Y.; Li, C.; Liu, Z.; Li, T.; Jiang, L. Asymmetrical [1]Benzothieno[3,2-*b*][1]Benzothiophene (BTBT) Derivatives for Organic Thin-Film and Single-Crystal Transistors. *Org. Electron.* **2020**, *77*, 105537.
(69) Mori, T.; Nishimura, T.; Yamamoto, T.; Doi, I.; Miyazaki, E.; Osaka, I.; Takimiya, K. Consecutive Thiophene-Annulation Approach to π-Extended Thienoacene-Based Organic Semiconductors with [1]Benzothieno[3,2-*b*][1]Benzothiophene (BTBT) Substructure. *J. Am. Chem. Soc.* **2013**, *135*, 13900–13913.
(70) Abe, M.; Mori, T.; Osaka, I.; Sugimoto, K.; Takimiya, K. Thermally, Operationally, and Environmentally Stable Organic Thin-Film Transistors Based on Bis[1]Benzothieno[2,3-*d*:2′,3′-*d*′]Naphtho[2,3-*b*:6,7-*b*′]Dithiophene Derivatives: Effective Synthesis, Electronic Structures, and Structure–Property Relations. *Chem. Mater.* **2015**, *27*, 5049–5057.
(71) Diele, S.; Tosch, S.; Mahnke, S.; Demus, D. Structure and Packing in Smectic E and Smectic A Phases in the Series of 4-n-Alkyloxy-4′-Alkanoylbiphenyls. *Cryst. Res. Technol.* **1991**, *26*, 809–817.
(72) Saito, K.; Miyazawa, T.; Fujiwara, A.; Hishida, M.; Saitoh, H.; Massalska-Arodź, M.; Yamamura, Y. Reassessment of Structure of Smectic Phases: Nano-Segregation in Smectic E Phase in 4- n -Alkyl-4′-Isothiocyanato-1,1′-Biphenyls. *J. Chem. Phys.* **2013**, *139*, 114902.
(73) Miyazawa, T.; Yamamura, Y.; Hishida, M.; Nagatomo, S.; Massalska-Arodź, M.; Saito, K. Revisiting Smectic E Structure through Swollen Smectic E Phase in Binary System of 4-Nonyl-4′-Isothiocyanatobiphenyl (9TCB) and n-Nonane. *J. Phys. Chem. B* **2013**, *117*, 8293–8299.
(74) Yoneya, M. Monolayer Crystal Structure of the Organic Semiconductor 7-Decyl-2-Phenyl[1]Benzothieno[3,2-*b*][1]Benzothiophene. *J. Phys. Chem. C* **2018**, *122*, 22225–22231.
(75) Inoue, S.; Nikaido, K.; Higashino, T.; Arai, S.; Tanaka, M.; Kumai, R.; Tsuzuki, S.; Horiuchi, S.; Sugiyama, H.; Segawa, Y.; Takaba, K.; Maki-Yonekura, S.; Yonekura, K.; Hasegawa, T. Emerging Disordered Layered-Herringbone Phase in Organic Semiconductors Unveiled by Electron Crystallography. *Chem. Mater.* **2022**, *34*, 72–83.
(76) Nikaido, K.; Inoue, S.; Kumai, R.; Higashino, T.; Matsuoka, S.; Arai, S.; Hasegawa, T. Mixing-Induced Orientational Ordering in Liquid-Crystalline Organic Semiconductors. *Adv. Mater. Interfaces* **2022**, *9*, 2201789.
(77) Fortunato, G.; Migliorato, P. Model for the Above-threshold Characteristics and Threshold Voltage in Polycrystalline Silicon Transistors. *J. Appl. Phys.* **1990**, *68*, 2463–2467.
(78) Horowitz, G.; Hajlaoui, R.; Bouchriha, H.; Bourguiga, R.; Hajlaoui, M. The Concept of "Threshold Voltage" in Organic Field-Effect Transistors. *Adv. Mater.* **1998**, *10*, 923–927.
(79) Tsuzuki, S.; Honda, K.; Uchimaru, T.; Mikami, M.; Tanabe, K. Origin of Attraction and Directionality of the π/π Interaction: Model Chemistry Calculations of Benzene Dimer Interaction. *J. Am. Chem. Soc.* **2002**, *124*, 104–112.
(80) Tsuzuki, S.; Honda, K.; Uchimaru, T.; Mikami, M. Estimated MP2 and CCSD(T) Interaction Energies of n-Alkane Dimers at the Basis Set Limit: Comparison of the Methods of Helgaker et Al. and Feller. *J. Chem. Phys.* **2006**, *124*, 114304.
(81) Matsuoka, S.; Ogawa, K.; Ono, R.; Nikaido, K.; Inoue, S.; Higashino, T.; Tanaka, M.; Tsutsumi, J.; Kondo, R.; Kumai, R.; Tsuzuki, S.; Arai, S.; Hasegawa, T. Highly Stable and Isomorphic Donor–Acceptor Stacking in a Family of n-Type Organic Semiconductors of BTBT–TCNQ Derivatives. *J. Mater. Chem. C* **2022**, *10*, 16471–16479.
(82) Arai, S.; Morita, K.; Tsutsumi, J.; Inoue, S.; Tanaka, M.; Hasegawa, T. Layered-Herringbone Polymorphs and Alkyl-Chain Ordering in Molecular Bilayer Organic Semiconductors. *Adv. Funct. Mater.* **2020**, *30*, 1906406.
(83) Arai, S.; Inoue, S.; Tanaka, M.; Tsuzuki, S.; Kondo, R.; Kumai, R.; Hasegawa, T. Temperature-Induced Transformation between Layered Herringbone Polymorphs in Molecular Bilayer Organic Semiconductors. *Phys. Rev. Mater.* **2023**, *7*, 025602.
(84) CrysAlisPro Software System, Rigaku Oxford Diffraction, Rigaku Corporation, Oxford, UK, 2016.
(85) Sheldrick, G. M. SHELXT - Integrated Space-Group and Crystal-Structure Determination. *Acta Crystallogr. Sect. A Found. Crystallogr.* **2015**, *71*, 3–8.
(86) Sheldrick, G. M. A Short History of SHELX. *Acta Crystallogr. Sect. A Found. Crystallogr.* **2008**, *64*, 112–122.
(87) Dolomanov, O. V.; Bourhis, L. J.; Gildea, R. J.; Howard, J. A. K.; Puschmann, H. OLEX2: a complete structure solution, refinement and analysis program. *J. Appl. Crystallogr.* **2009**, *42*, 339–341.
(88) Takaba, K.; Maki-Yonekura, S.; Inoue, I.; Tono, K.; Hamaguchi, T.; Kawakami, K.; Naitow, H.; Ishikawa, T.; Yabashi, M.; Yonekura, K. Structural Resolution of a Small Organic Molecule by Serial X-Ray Free-Electron Laser and Electron Crystallography. *Nat. Chem.* **2023**, *15*, 491–497.
(89) Tono, K.; Togashi, T.; Inubushi, Y.; Sato, T.; Katayama, T.; Ogawa, K.; Ohashi, H.; Kimura, H.; Takahashi, S.; Takeshita, K.; Tomizawa, H.; Goto, S.; Ishikawa, T.; Yabashi, M. Beamline, Experimental Stations and Photon Beam Diagnostics for the Hard X-Ray Free Electron Laser of SACLA. *New J. Phys.* **2013**, *15*, 083035.
(90) White, T. A.; Mariani, V.; Brehm, W.; Yefanov, O.; Barty, A.; Beyerlein, K. R.; Chervinskii, F.; Galli, L.; Gati, C.; Nakane, T.; Tolstikova, A.; Yamashita, K.; Yoon, C. H.; Diederichs, K.; Chapman, H. N. Recent Developments in CrystFEL. *J. Appl. Crystallogr.* **2016**, *49*, 680–689.
(91) Spek, A. L. Single-crystal structure validation with the program PLATON. *J. Appl. Crystallogr.* **2003**, *36*, 7−13.

(92) Takaba, K.; Maki-Yonekura, S.; Inoue, S.; Hasegawa, T.; Yonekura, K. Protein and Organic-Molecular Crystallography With 300kV Electrons on a Direct Electron Detector. *Front. Mol. Biosci.* **2021**, *7*, No. 612226.
(93) Mastronarde, D. N. Automated electron microscope tomography using robust prediction of specimen movements. *J. Struct. Biol.* **2005**, *152*, 36–51.
(94) Yonekura, K.; Ishikawa, T.; Maki-Yonekura, S. A new cryo-EM system for electron 3D crystallography by eEFD. *J. Struct. Biol.* **2019**, *206*, 243–253.
(95) Clabbers, M. T. B.; Gruene, T.; Parkhurst, J. M.; Abrahams, J. P.; Waterman, D. G. Electron diffraction data processing with DIALS. A*cta Crystallogr. D Struct. Biol.* **2018**, *74*, 506–518.
(96) McCoy, A. J.; Grosse-Kunstleve, R. W.; Storoni, L. C.; Read, R. J. Likelihood-enhanced fast translation functions. *Acta Crystallogr.* **2005**, *D61*, 458–464.
(97) Giannozzi, P. *et al.* QUANTUM ESPRESSO: A Modular and Open-Source Software Project for Quantum Simulations of Materials. *J. Phys. Condens. Matter* **2009**, *21*, 395502.
(98) Giannozzi, P. *et al.* Advanced capabilities for materials modelling with Quantum ESPRESSO. *J. Phys. Condens. Matter* **2017**, *29*, 465901.
(99) Perdew, J. P.; Burke, K.; Ernzerhof, M. Generalized Gradient Approximation Made Simple. *Phys. Rev. Lett.* **1996**, *77*, 3865–3868.
(100) Grimme, S.; Antony, J.; Ehrlich, S.; Krieg, H. A Consistent and Accurate Ab Initio Parametrization of Density Functional Dispersion Correction (DFT-D) for the 94 Elements H-Pu. *J. Chem. Phys.* **2010**, *132*, 154104.
(101) Dennington, R.; Keith, T.; Millam, J.; *GaussView, version 5.0*, Semichem Inc., Shawnee Mission, KS, **2009**.
(102) Becke, A. D. Density-functional Thermochemistry. III. The Role of Exact Exchange. *J. Chem. Phys.* **1993**, *98*, 5648–5652.
(103) Frisch, M. J. *et al. Gaussian 16*, Wallingford, CT, **2016**.
(104) Ransil, B. J. Studies in Molecular Structure. IV. Potential Curve for the Interaction of Two Helium Atoms in Single-Configuration LCAO MO SCF Approximation. *J. Chem. Phys.* **1961**, *34*, 2109–2118.
(105) Boys, S. F.; Bernardi, F. The Calculation of Small Molecular Interactions by the Differences of Separate Total Energies. Some Procedures with Reduced Errors. *Mol. Phys.* **1970**, *19*, 553–566.
(106) Stone, A. J.; Dullweber, A.; Hodges, M. P.; Popelier, P. L. A.; Wales, D. J. *ORIENT 3.2: A Program for Studying Interactions between Molecules Version 3.2*, University of Cambridge, **1995**.
(107) Stone, A. J.; Alderton, M. Distributed multipole analysis. *Mol. Phys.* **1985**, *56*, 1047–1064.
(108) Stone, A. J. Distributed Multipole Analysis: Stability for Large Basis Sets. *J. Chem. Theory Comput.* **2005**, *1*, 1128–1132.
(109) Stone, A. J. Distributed Polarizabilities. *Mol. Phys.* **1985**, *56*, 1065–1082.
(110) van Duijnen, P. T.; Swart, M. Molecular and Atomic Polarizabilities: Thole's Model Revisited. *J. Phys. Chem. A* **1998**, *102*, 2399–2407.
(111) Rühle, V.; Lukyanov, A.; May, F.; Schrader, M.; Vehoff, T.; Kirkpatrick, J.; Baumeier, B.; Andrienko, D. Microscopic Simulations of Charge Transport in Disordered Organic Semiconductors. *J. Chem. Theory Comput.* **2011**, *7*, 3335–3345.
(112) Brédas, J.-L.; Beljonne, D.; Coropceanu, V.; Cornil, J. Charge-Transfer and Energy-Transfer Processes in π-Conjugated Oligomers and Polymers: A Molecular Picture. *Chem. Rev.* **2004**, *104*, 4971–5004.